PCCP

Accepted Manuscript

ROYAL SOCIETY OF CHEMISTRY

www.rsc.org/pccp

Journal Name

ARTICLE TYPE

Cite this: DOI: 10.1039/xxxxxxxxxx

Mechanisms and Dynamics of Protonation and Lithiation of Ferrocene[†]

Nishant Sharma, Jayanth K. Ajay,[‡] Krishnan Venkatasubbaiah and Upakarasamy Lourderaj[*]

Received Date
Accepted Date

DOI: 10.1039/xxxxxxxxxx

www.rsc.org/journalname

Elucidating the mechanism of the simplest electrophilic substitution reaction of ferrocene, the protonation reaction has been a difficulty. In the work reported here, ab initio chemical dynamics simulations were performed at B3LYP/DZVP level of theory to understand the atomic level mechanisms of protonation and lithiation of ferrocene. Protonation of ferrocene resulted in the agostic and metal-protonated forms. Trajectory calculations revealed that protonation of ferrocene occurs by exo and endo mechanisms, with exo being the major path. H^+ was found to be mobile and hopped from the Cp ring to the metal center and vice-versa after the initial attack on ferrocene, with the metal-complex having a shorter lifetime. These results remove the ambiguity surrounding the mechanism, as proposed in earlier experimental and computational studies. Lithiation of ferrocene resulted in the formation of cation-π and metal-lithiated complexes. Similar to protonation, trajectory results revealed that both exo and endo paths were followed, with exo path being the major. In addition, lithiated-ferrocene exhibited planetary motion. The major path (exo) followed in the protonation and lithiation of ferrocene is consistent with the observations in earlier experimental studies for other hard electrophiles.

1 Introduction

Ferrocene undergoes reactions characteristic of aromatic compounds by which plenty of its derivatives, which have potential applications in various fields, have been synthesized[1–5]. Some of the most interesting reactions of ferrocene are the electrophilic substitution reactions as seen in Friedel-Crafts reaction[6–8] and mercuration[9]. The mechanism of electrophilic substitution of ferrocene was investigated by a series of studies by Cunningham using mass-spectrometry and isotopic substitution[7–9], and two possible mechanisms were proposed (Fig. 1). It was found that hard electrophiles such as CH_3CO^+ followed an exo mechanism where the electrophiles are expected to attack ferrocene on the exo face of the cyclopentadienyl (Cp) ring (Exo attack), while soft electrophiles such as Hg^{2+} first complexed with the metal atom and then attacked the Cp ring on its endo face (Endo attack).

However, if the electrophile is a proton (H^+), the intermediates formed after exo and endo attacks are indistinguishable, and an experimental verification of the mechanism becomes a difficulty. Several experimental[10–15] and theoretical[16–19] studies were performed to understand the mechanism of protonation of ferrocene. The protonation of ferrocene can result in a metal-protonated form (**MP**), where H^+ is attached to the Fe atom, or a ring protonated complex called “agostic form” (**AG**), where an H atom forms a three-centered bond.

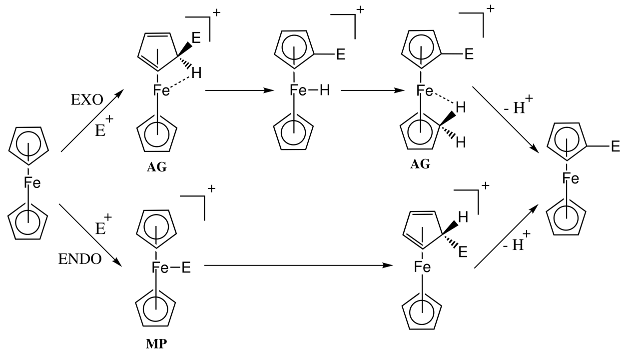

Fig. 1 Exo and endo pathways for electrophilic substitution reaction of ferrocene.

NMR studies[10,11] showed that only metal-protonated form is present in solution. Deuteriation experiments in the gas-phase suggested that the incoming H^+/D^+ attaches to Fe or Cp ring and does not exchange with the Cp hydrogens[12]. In contrast, experiments in deuterated acidic media indicated an exo attack

---

School of Chemical Sciences, National Institute of Science Education and Research, Bhubaneswar, Odisha, INDIA.

[†] Electronic Supplementary Information (ESI) available: Computational details, Tables S1-S3 and Figures S1-S8. See DOI: 10.1039/b000000x/

[‡] Present address: Fritz Haber Research Center for Molecular Dynamics, Hebrew University of Jerusalem, Jerusalem 91904, Israel.

and a possibility of rapid equilibrium between ring and metal-protonated forms of ferrocene[13]. Infrared spectroscopic studies on protonated ferrocene revealed the presence of Fe–H stretching and Cp–Fe–H deformation motions.[14] In another gas-phase study, H atom switching from one Cp ring to another and scrambling of H atoms in Cp rings were suggested[15].

Although there have been several theoretical studies in understanding the mechanism of protonation of ferrocene, most of the studies involved mapping the stationary points on the potential energy surface (PES) of protonated ferrocene[16–19] and are summarized in Fig. S1. It was found that the nature of the PES was sensitive to the level of theory. At the HF level with effective core potential (ECP) for iron and 6-31G* for other atoms, **MP** was lower in energy than **AG** by 58 kcal/mol, whereas MP2 showed that **AG** was more stable than **MP** by 35 kcal/mol[16]. Density functional theoretical (DFT) study using BPW91 and triple-ζ STO basis set[17] indicated a shallow PES with **MP** more stable than **AG** only by 0.3 kcal/mol. CCSD(T)/pVDZ calculations revealed that **AG** was more stable than **MP** by 2.1 kcal/mol[19]. Recently, a detailed study of the structure and dynamics of protonated ferrocene was performed using BP86, BPW91, BLYP, and B3LYP functionals and various basis sets. It was found that B3LYP predicted **AG** to be more stable than **MP** by 2-4 kcal/mol for different basis sets,[18] comparable to CCSD(T)/pVDZ values. The ab initio (B3LYP) molecular dynamics study of protonated ferrocene revealed that **AG** was more preferred, while the computed ^{57}Fe and ^{1}H NMR chemical shifts were closer to the experimental chemical shifts of **MP** and **AG** respectively.[18] The various experimental and theoretical studies revealed the importance of agostic structure in the protonation of ferrocene; however, the preference for exo or endo attack could not be clearly established. Interestingly, the next higher analogous hard electrophile Li$^+$ can be expected to follow an exo mechanism. Although there are no experimental studies reported on the mechanism of lithiation of ferrocene, DFT studies[20,21] have shown that Li$^+$ binds strongly to the top of the Cp ring than to the metal and that the metal-lithiated complex can exhibit a “planetary motion”.

Here, a detailed ab initio chemical dynamics simulation study was undertaken to understand the atomic level mechanism and dynamics of protonation and lithiation of ferrocene. To this end, the PESs for protonation and lithiation of ferrocene were mapped using B3LYP/DZVP[22–25] level of theory. To understand the dynamics, ab initio classical trajectories were integrated “on-the-fly” at the B3LYP/DZVP level of theory.

2 Computational Methods

The potential energy profiles for protonated and lithiated ferrocene were mapped using B3LYP[22,23] and BPW91[26,27] functionals and DZVP[24,25] basis set. The stationary point structures were characterized by computing harmonic vibrational frequencies. GAUSSIAN 09[28] and NWChem[29] software were used to carry out these calculations. All the energies reported here are without zero-point-energy correction.

Ab initio classical trajectories[30–32] were performed to understand the unimolecular as well as the bimolecular dynamics of protonation and lithiation of ferrocene using VENUS/NWChem[33], where the ab initio forces were computed at B3LYP/DZVP level of theory. Since B3LYP/DZVP results were closer to CCSD(T)/pVDZ[19], the trajectories were calculated using this level of theory. The initial coordinates and momenta were selected using quasi-classical sampling procedure.[34] The trajectories were integrated numerically for 0.5-1 ps using velocity-Verlet algorithm[35]. The typical CPU time for $\sim$1 ps integration of a trajectory on a 8 core Intel Xeon (3.0 GHz) processor is $\sim$6 days. Detailed computational procedure is given in ESI.

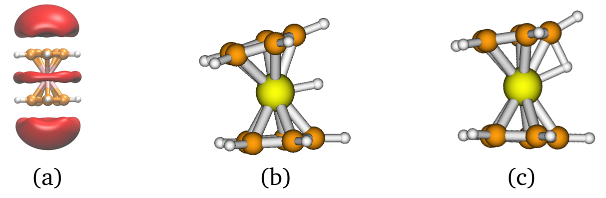
(a) (b) (c)

Fig. 2 (a) Iso-electrostatic (-0.013 a.u) potential map for ferrocene. (b) and (c) Minimum energy structures of **MP** and **AG** respectively, at B3LYP/DZVP level of theory.

3 Results and discussion

3.1 Protonation of Ferrocene

The molecular electrostatic potential (MEP) map for the value of -0.013 a.u is shown in Fig. 2a. The presence of negative potential above and below the Cp rings and around the Fe atom indicates the possible protonation and lithiation sites of ferrocene. As discussed above, protonation of ferrocene can result in **MP** or **AG** (Fig. 2b and 2c). Tables S1 and S2 compare the important geometrical parameters and energies of neutral ferrocene and the stationary points on the PES of protonated ferrocene calculated at BPW91[26,27]/6-311++G**, B3LYP/6-311++G**, and B3LYP/DZVP levels of theory. Neutral ferrocene has D_{5h} symmetry, and the geometrical parameters are in good agreement with the experimental ones. As reported in the literature, two minima - **MP** and **AG** were obtained for protonated ferrocene. At the B3LYP/DZVP level of theory, **AG** is more stable than **MP** by 2.58 kcal/mol consistent with the reported CCSD(T) values[19]. It must be noted that the effect of diffusion functions (6-311++G**) on the geometry and energies was found to be negligible. Here, we discuss the results obtained using B3LYP/DZVP level of theory.

Fig. 3 shows the possible stationary points on the PES of protonated ferrocene at the B3LYP/DZVP level of theory. **AG** and **MP** are connected by a transition state (**TSa**), 2.63 kcal/mol above **AG**. In **AG**, the Cp rings are eclipsed and H$^+$ forms a three-centered bond with Fe and one of the C atoms of Cp ring. The Fe-H distance is 1.70 Å and angle subtended by the center of mass of the Cp ring (X_1), Fe and H ($\angle X_1$-Fe-H) is 74°. In addition, **AG** can also exist in isoenergic conformers (rotamers) formed by rotation of Cp rings connected to each other by a transition state (**TSb**), with a barrier of 0.31 kcal/mol. In **MP**, H is attached to the metal ring. The Fe-H distance is 1.49 Å and $\angle X_1$-Fe-H is 97°. The isoenergic rotamers formed by Cp ring rotation are connected by a transition state (**TSc**), 2.58 kcal/mol above **MP**. The Fe-H distance is shorter in **MP** (1.49 Å) than it is in **AG** (1.70 Å) at the

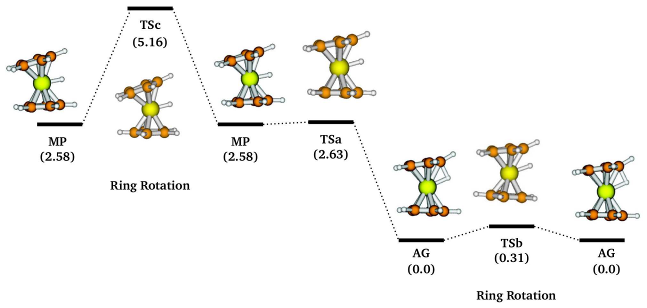

Fig. 3 Potential energy profile of protonated ferrocene calculated at B3LYP/DZVP level of theory. Energies (kcal/mol) relative to **AG** are given in parenthesis.

B3LYP/DZVP level of theory. However, endo C-H distance is short in **AG** as compared to **MP**. In addition, the exo H atom in **AG** can hop from one C atom to another *via* **TSd** that is 20.29 kcal/mol above **AG** (Fig. S2a). The MEP map (Fig. S2b) shows that the positive charge is more on both the exo and endo H atoms in **AG** and on the H atom attached to Fe in **MP**.

The dynamics of protonation of ferrocene was investigated by performing classical trajectory simulations at the B3LYP/DZVP level of theory. As a first step, the dynamics of protonated ferrocene was studied by following the trajectories initiated at **AG** and **MP** minima with Boltzmann distribution of vibrational and rotational energies at 300 K. 50 trajectories were initiated from **AG**, and 45 trajectories were initiated from **MP** and integrated for 1.5-2 ps.

3.1.1 Dynamics of Protonated Ferrocene

Once ferrocene is protonated on one of the Cp rings (Cp_1), H^+ can hop to the Fe atom and back to the starting Cp ring (Cp_1) or to the other Cp ring (Cp_2). 41 of 50 trajectories initiated from agostic minimum showed H^+ hopping between the Cp rings and Fe atom. The remaining 9 trajectories were trapped in **AG** for 1.5 ps. 39 of 45 trajectories initiated from metal-protonated minimum showed isomerization between **AG** and **MP**, and the remaining 7 trajectories were trapped in **AG**. Interestingly, none of the trajectories were trapped in **MP**. Most trajectories showed H^+ hopping between the Cp rings, suggesting the existence of rapid isomerization between the two forms. In 3 trajectories initiated at **AG** and 11 trajectories initiated at **MP**, hopping of H^+ on different carbon atoms of the same Cp ring was seen. The hopping of H^+ between the C atoms of the ring happens *via* **MP**. In addition, most of the trajectories exhibited rotation of Cp rings relative to each other during the course of the trajectory.

The lifetimes of **AG** and **MP** were calculated by following X_1-Fe-H angle as a function of time. The lifetime distributions (Figs. 4 and S3) have a nearly exponentially decaying behavior. The population of **AG**s with large lifetime of 1.5 ps corresponds to trapped trajectories. However, they are expected to isomerize to **MP** if integrated for longer times. For trajectories initiated at **AG**, the computed average lifetimes for **AG** and **MP** were found to be 186 fs and 16 fs respectively, and for trajectories initiated at **MP**, the computed average lifetimes for **AG** and **MP** were found to be 167 fs and 17 fs respectively. This suggests that H^+ spends most of the time attached to one of the C atoms of the Cp ring rather than Fe atom.

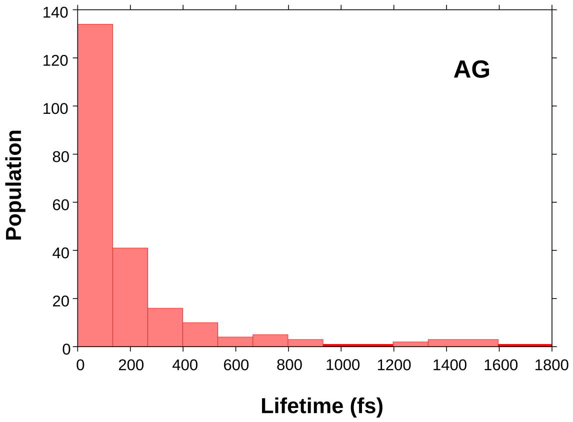

Fig. 4 Plot of population vs lifetime for **AG** when the trajectories were initiated from agostic minimum.

3.1.2 Dynamics of Protonation of Ferrocene

To understand the mechanism of protonation of ferrocene, it is important to know the intial attack of H^+ on ferrocene (i.e., Exo or Endo attack). The reaction mechanism was investigated by following bimolecular collision trajectories. However, trajectories initiated with ferrocene and H^+ separated by 8 Å apart, failed due to the instability of the density. Hence, to mimick the bimolecular collisions, trajectories were initiated using three partially optimized structures (Fig. S4) obtained by fixing (i) the endo C-H distance at 5 Å in **AG**, (ii) H^+ on top of the Cp ring with $\angle X_1$-Fe-H = 4.6° and Fe-H at 6.6 Å (iii) $\angle X_1$-Fe-H at 41.8° and Fe-H at 7.48 Å. A total of 182 trajectories were initiated with different orientations of H^+ about ferrocene with Boltzmann distribution of energies at 300 K and integrated typically for 0.5–1 ps. 80 of those trajectories resulted in protonation of ferrocene, and their initial orientations with respect to ferrocene are plotted in Fig. 5a.

Details of the atomistic mechanisms can be obtained following the motion of the attacking H^+ in the trajectories. It was found that in 58 of 80 trajectories, the initial attack of H^+ was on top of the Cp ring (Exo path), and 22 trajectories followed Endo path. Three representative trajectories showing different attacks are shown in Fig. 5b. The protonation reaction showed interesting dynamical features. 35 of the 58 trajectories that followed exo path showed hopping of H^+ on the C atoms of the protonated Cp ring, after the initial attack of H^+ on one of the C atoms of the ring. A representative trajectory is shown in Fig. 6a. In 23 of these 32 trajectories, after hopping, the protonated C atom transferred the endo H^+ to the other Cp ring *via* **MP**. In the remaining 9 trajectories, H^+ hopped between the C atoms of the Cp ring; however, the protonated ferrocene stayed in **AG**. Another 19 of

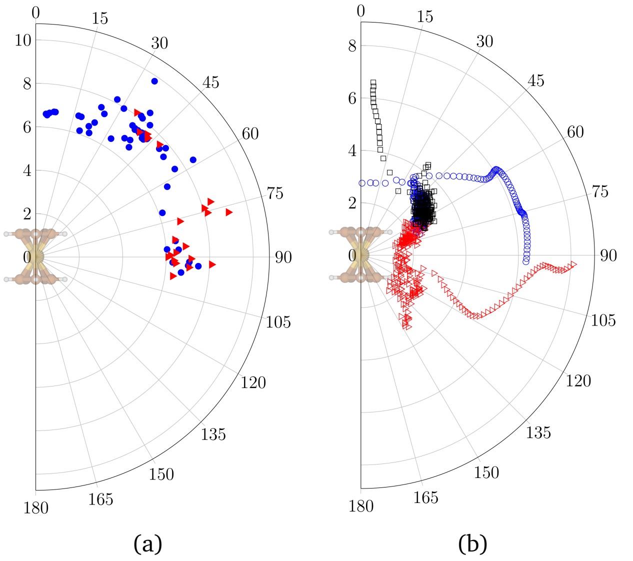

(a) (b)

Fig. 5 Polar plots of $\angle X_1$-Fe-H(°) vs Fe-H distance(Å). (a) Initial orientation of H^+ in 80 trajectories is shown. Filled blue circles (●) are orientations that resulted in exo attack and filled red triangles (▶) are those that showed endo attack. (b) Black squares (☐) and blue circles (○) represent two trajectories showing exo attack; red triangles (▷) represent a trajectory showing endo attack. Ferrocene is superimposed for qualitative description.

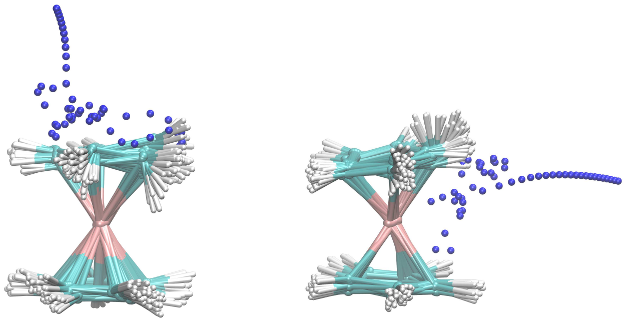

(a) (b)

Fig. 6 Representative trajectories (with frames superimposed) for 175 fs showing (a) exo attack and H^+ hopping on the CP ring and (b) endo attack and H^+ hopping between the two Cp rings. H^+ is shown in blue for clarity.

58 trajectories following exo path transferred the endo H^+ of the protonated C atom to the other ring soon after the attack. 4 of the 58 exo-path trajectories stayed in **AG** for the complete integration time without hopping on the C atoms of the Cp ring. Interestingly, all the 22 trajectories that followed endo path showed similar behavior. In all the trajectories, hopping of H^+ from one Cp ring to the other through **MP** was seen. A representative trajectory is shown in Fig. 6b.

It is interesting to investigate if the initial orientation of H^+ with respect to ferrocene has any effect on the exo and endo mechanisms seen. A plot of $\angle X_1$-Fe-H (Fig. 5a) for the 80 trajectories shows that the initial orientation covers the full range of angles between 0° and 105°. It can be seen that the trajectories that follow exo path do not show any preference with respect to initial orientation. However, the trajectories following endo path are those that were initiated with $\angle$X-Fe-H between 45° and 105°, indicating a possible orientational preference for endo mechanism.

3.2 Lithiation of Ferrocene

It is of fundamental interest to understand the nature of the mechanism for the next higher electrophile, Li^+. Since Li^+ is a hard electrophile, it is expected that lithiation would follow the exo path. The top of the Cp ring of ferrocene has a more negative MEP value (Fig. S5) than the radial region, showing that the probability of Li^+ binding in the top region is more than that in the radial region. Fig. 7 shows the PES with relative energies for lithiated ferrocene obtained at B3LYP/DZVP level of theory. Lithiation of ferrocene results in two isomers: an on-top cation-π complex (**CP**) and a metal-lithiated complex (**ML**) that is 7.05 kcal/mol higher in energy than **CP**. The geometrical parameters and relative energies of the stationary points on the PES of lithiated ferrocene are reported in Table S3.

In **CP**, Li atom is at the center of the Cp ring and hence equidistant (2.32 Å) from the five C atoms of the Cp ring. In **ML**, the Fe-Li distance is 2.46 Å, and Li atom is staggered with respect to the closest Cp ring C atoms ($\angle$Li-Fe-X_1-C = 44°). The MEP map (Fig. S6) shows that the positive charge is more around the Li atom. **CP** and **ML** are connected by a transition state **TSe** that is 23.62 kcal/mol above **CP**. In **TSe**, the Li atom lies in the plane of the Cp ring and is located perpendicular to the center of the nearest C-C bonds. Interestingly, the **ML** isomer can isomerize to five isoenergic symmetrical forms with Li^+ atom moving about the Fe atom. Two neighboring isoenergic forms along the intrinsic reaction coordinate (IRC) are connected by a transition state **(TSf)** with a barrier height of 1.47 kcal/mol. The motion along the IRC connecting the isoenergic minima (with no rotation of Cp rings relative to each other) represents a "planetary" system with Li^+ atom revolving around the Fe atom. It is to be noted that each **ML** along the IRC can exist in five more isoenergic isomers formed by rotation of Cp rings relative to each other and

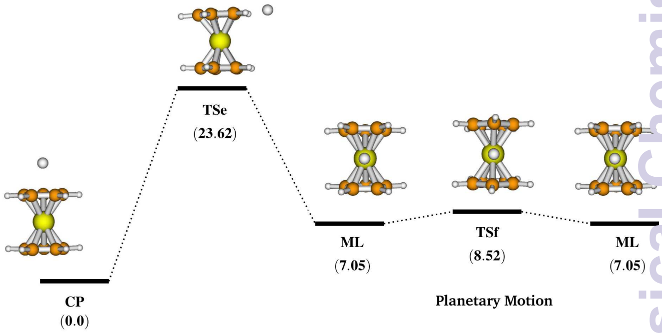

Fig. 7 Potential energy profile of lithiated ferrocene calculated at B3LYP/DZVP level of theory. Energies (kcal/mol) relative to **CP** are given in parenthesis.

connected by **TSg** (Fig. S7) with a barrier of 1.03 kcal/mol.

3.2.1 Dynamics of Lithiated Ferrocene

Similar to protonation of ferrocene, ab initio classical trajectory simulations were performed to understand the dynamics and mechanism of lithiation of ferrocene. 25 trajectories were initiated from the transition state **TSf** along the IRC for planetary motion with a Bolztmann distribution of vibrational and rotational energies at 300 K and integrated typically for 1–1.5 ps. Some trajectories exhibited a complete planetary motion of Li$^+$ around Fe atom and did not show ring rotation. In others, the planetary motion was incomplete, and they exhibited relative Cp ring rotations. During the planetary motion, Fe–Li distance oscillates about the equilibrium distance of 2.45 Å, indicating that Li$^+$ is bound to Fe atom during the motion (Fig. S8). A set of 5 trajectories was also initiated at transition state **TSe** and integrated for 1.5 ps. In these trajectories, the Li$^+$ either migrated to Fe atom and then followed a planetary motion via **TSf** or formed **CP** and stayed in the minimum until the integration time of 1.5 ps.

3.2.2 Dynamics of Lithiation of Ferrocene

To understand the atomic-level mechanism of lithiation of ferrocene and the preferred initial binding site of Li$^+$ cation in ferrocene, bimolecular collisions between ferrocene and Li$^+$ were followed. 80 trajectories were initiated at a relative distance of 8 Å with a Boltzmann distribution of vibrational and rotational energies of ferrocene at 300 K with initial $\angle X_1$-Fe-Li in the range 0°-90° (Fig. 8a). The trajectories were integrated typically for 0.5–1.5 ps, and an impact parameter (b) of zero was used for effective collisions. The trajectories indicated that Li$^+$ was quite mobile similar to H$^+$ in protonation. Of the 80 trajectories, 67 trajectories showed an exo attack of Li$^+$ forming **CP**, and the remaining 13 trajectories showed Li$^+$ atom exhibiting endo attack forming **ML**. Three representative trajectories showing different attacks are shown in Fig. 8b. In 56 of those trajectories that followed exo path, the system remained in **CP** minimum for the integration time, and in the remaining 11 trajectories the system isomerized to **ML** from **CP**. 2 of these 11 trajectories exhibited planetary motion after **ML** formation. A representative trajectory is shown in Fig. 9a. The 13 trajectories that followed endo mechanism formed **ML** and exhibited interesting dynamics. 3 of these trajectories stayed in **ML** minimum for the integration time. 1 trajectory exhibited planetary motion after forming **ML**. In 5 of the trajectories, the system isomerized from **ML** to **CP** and remained in the **CP** minimum. In 2 other trajectories, the system isomerized from **ML** to **CP** and back to **ML** and then exhibited planetary motion. A representative trajectory is shown in Fig. 9b. A few trajectories calculated with $b = 2$ and $b = 5$ (8 each) also showed similar dynamical features and followed exo path.

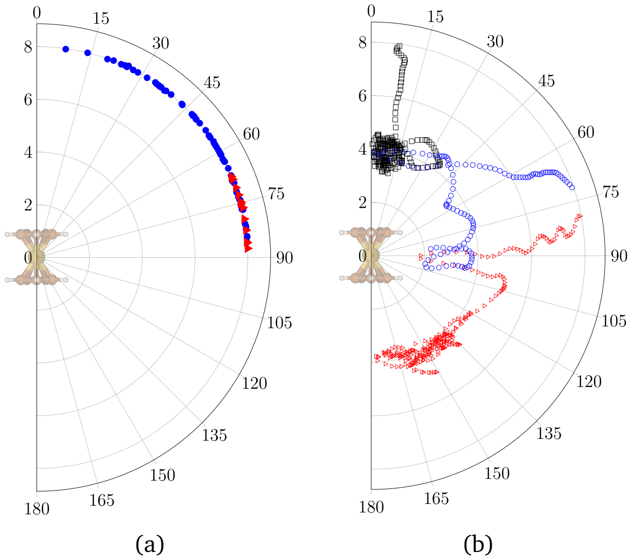

(a) (b)

Fig. 8 Polar plots of $\angle X_1$-Fe-Li(°) vs Fe-Li distance (Å). (a) Initial orientation of Li$^+$ in 80 trajectories is shown. Filled blue circles (●) are orientations that resulted in exo attack and filled red triangles (▶) are those that showed endo attack. (b) Black squares (☐) and blue circles (○) represent two trajectories showing exo attack; red triangles (▷) represent a trajectory showing endo attack. Ferrocene is superimposed for qualitative description.

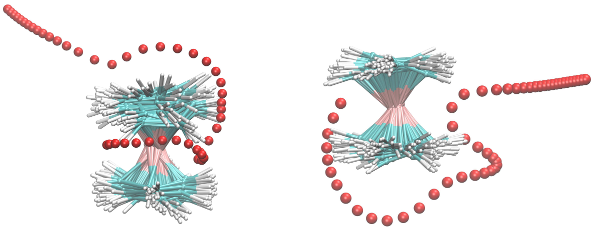

(a) (b)

Fig. 9 Representative trajectories (with frames superimposed) for (a) 675 fs showing exo attack followed by the planetary motion and (b) 735 fs showing endo attack followed by the formation of **CP** and then **ML** *via* **TSd**. Li$^+$ is shown in red for clarity.

The plot of the initial Li$^+$ orientation with respect to ferrocene ($\angle X_1$-Fe-Li, Fig. 8a) shows that for those trajectories that followed exo path, $\angle X_1$-Fe-Li is distributed over the full range of 0°-90°. However, the trajectories following endo path have $\angle X_1$-Fe-Li between 65°-90°. Clearly, an orientational preference ($\angle X_1$-Fe-Li > 65°) is seen for the endo path.

4 Conclusions

Ab initio chemical dynamics simulations were performed at B3LYP/DZVP level of theory to understand the atomic level mechanisms of protonation and lithiation of ferrocene. The results indicate that in both protonation and lithiation, the major path followed is the exo path. It was found that the exo path did not depend on initial orientation of the approaching electrophile, however, in the endo path, an orientational preference of the approaching electrophile was seen. The electrophile was found to be very mobile and hopped from the Cp ring to the metal center and vice-versa after the initial attack on ferrocene, with the metal-complex having a very short lifetime. This explains the experimental observations[10,11,15] in the study of protonation of ferrocene, suggesting the coexistence of metal-protonated and agostic forms and H atom switching from one ring to another including scrambling of H atoms in Cp rings and the difficulty in understanding the mechanism unequivocally. The major path (exo) followed in the protonation and lithiation of ferrocene, as seen in the simulations, is consistent with the observations of Cunningham for other hard electrophiles[7–9]. In addition, during lithiation a planetary motion of Li atom around Fe atom was also observed.

Acknowledgements

The authors thank NISER, Bhubaneswar for computational facility. This work was partially supported by Department of Science and Technology (SR/S1/PC/0060/2010, SR/S2/RJN-49/2011 and SR/S1/IC-58/2012), India.

References

1 A. Togni and T. Hayashi, *Ferrocenes: Homogeneous Catalysis, Organic Synthesis, Materials Science*, John Wiley & Sons, Inc., 2008.

2 P. Stepnicka, *Ferrocenes: Ligands, Materials and Biomolecules*, John Wiley & Sons, Inc., 2008.

3 D. R. van Staveren and N. Metzler-Nolte, *Chem. Rev.*, 2004, **104**, 5931–5986.

4 K. Heinze and H. Lang, *Organometallics*, 2013, **32**, 5623–5625.

5 H. Werner, *Angew. Chem. Int. Ed.*, 2012, **51**, 6052–6058.

6 S. Ahn, Y.-S. Song, B. R. Yoo and I. N. Jung, *Organometallics*, 2000, **19**, 2777–2780.

7 A. F. Cunningham, *J. Am. Chem. Soc.*, 1991, **113**, 4864–4870.

8 A. F. Cunningham, *Organometallics*, 1994, **13**, 2480–2485.

9 A. F. Cunningham, *Organometallics*, 1997, **16**, 1114–1122.

10 T. J. Curphey, J. O. Santer, M. Rosenblum and J. H. Richards, *J. Am. Chem. Soc.*, 1960, **82**, 5249–5250.

11 A. Karlsson, A. Broo and P. Ahlberg, *Can. J. Chem.*, 1999, **77**, 628–633.

12 M. Meot-Ner, *J. Am. Chem. Soc.*, 1989, **111**, 2830–2834.

13 U. T. Mueller-Westerhoff, T. J. Haas, G. F. Swiegers and T. K. Leipert, *J. Organomet. Chem.*, 1994, **472**, 229–246.

14 I. Pavlík and J. Šubrt, *Collection Czechoslov. Chem. Commun.*, 1967, **32**, 76–88.

15 C. Hop and T. McMahon, *J. Am. Soc. Mass Spectrom.*, 1994, **5**, 274–281.

16 M. L. McKee, *J. Am. Chem. Soc.*, 1993, **115**, 2818–2824.

17 M. J. Mayor-López, J. Weber, B. Mannfors and A. F. Cunningham, *Organometallics*, 1998, **17**, 4983–4991.

18 M. Bühl and S. Grigoleit, *Organometallics*, 2005, **24**, 1516–1527.

19 M. J. Mayor-López, H. P. Lüthi, H. Koch, P. Y. Morgantini and J. Weber, *J. Chem. Phys.*, 2000, **113**, 8009–8014.

20 A. Irigoras, J. M. Mercero, I. Silanes and J. M. Ugalde, *J. Am. Chem. Soc.*, 2001, **123**, 5040–5043.

21 J. Rodríguez-Otero, E. M. Cabaleiro-Lago, Ángeles Peña Gallego and M. M. Montero-Campillo, *Tetrahedron*, 2009, **65**, 2368–2371.

22 C. Lee, W. Yang and R. G. Parr, *Phys. Rev. B*, 1988, **37**, 785–789.

23 A. D. Becke, *J. Phys. Chem.*, 1993, **98**, 5648–5652.

24 N. Godbout, D. R. Salahub, J. Andzelm and E. Wimmer, *Can. J. Chem.*, 1992, **70**, 560–571.

25 C. Sosa, J. Andzelm, B. C. Elkin, E. Wimmer, K. D. Dobbs and D. A. Dixon, *J. Phys. Chem.*, 1992, **96**, 6630–6636.

26 A. D. Becke, *Phys. Rev. A*, 1988, **38**, 3098–3100.

27 J. P. Perdew and Y. Wang, *Phys. Rev. B*, 1992, **45**, 13244–13249.

28 M. J. Frisch, G. W. Trucks, H. B. Schlegel, G. E. Scuseria, M. A. Robb, J. R. Cheeseman, G. Scalmani, V. Barone, B. Mennucci, G. A. Petersson, H. Nakatsuji, M. Caricato, X. Li, H. P. Hratchian, A. F. Izmaylov, J. Bloino, G. Zheng, J. L. Sonnenberg, M. Hada, M. Ehara, K. Toyota, R. Fukuda, J. Hasegawa, M. Ishida, T. Nakajima, Y. Honda, O. Kitao, H. Nakai, T. Vreven, J. A. Montgomery, Jr., J. E. Peralta, F. Ogliaro, M. Bearpark, J. J. Heyd, E. Brothers, K. N. Kudin, V. N. Staroverov, R. Kobayashi, J. Normand, K. Raghavachari, A. Rendell, J. C. Burant, S. S. Iyengar, J. Tomasi, M. Cossi, N. Rega, J. M. Millam, M. Klene, J. E. Knox, J. B. Cross, V. Bakken, C. Adamo, J. Jaramillo, R. Gomperts, R. E. Stratmann, O. Yazyev, A. J. Austin, R. Cammi, C. Pomelli, J. W. Ochterski, R. L. Martin, K. Morokuma, V. G. Zakrzewski, G. A. Voth, P. Salvador, J. J. Dannenberg, S. Dapprich, A. D. Daniels, Ã. Farkas, J. B. Foresman, J. V. Ortiz, J. Cioslowski and D. J. Fox, *Gaussian09 Revision D.01*, Gaussian Inc. Wallingford CT 2009.

29 M. Valiev, E. Bylaska, N. Govind, K. Kowalski, T. Straatsma, H. V. Dam, D. Wang, J. Nieplocha, E. Apra, T. Windus and W. de Jong, *Comput. Phys. Commun.*, 2010, **181**, 1477–1489.

30 L. Sun and W. L. Hase, in *Born-Oppenheimer Direct Dynamics Classical Trajectory Simulations*, John Wiley & Sons, Inc., 2003, pp. 79–146.

31 U. Lourderaj, K. Song, T. L. Windus, Y. Zhuang and W. L. Hase, *J. Chem. Phys.*, 2007, **126**, 044105.

32 U. Lourderaj, K. Park and W. L. Hase, *Int. Rev. Phys. Chem.*, 2008, **27**, 361–403.

33 U. Lourderaj, R. Sun, S. C. Kohale, G. L. Barnes, W. A. de Jong, T. L. Windus and W. L. Hase, *Comput. Phys. Commun.*, 2014, **185**, 1074–1080.

34 G. H. Peslherbe, H. Wang and W. L. Hase, in *Monte Carlo Sampling for Classical Trajectory Simulations*, John Wiley & Sons, Inc., 2007, pp. 171–201.

35 D. Levesque and L. Verlet, *J. Stat. Phys.*, 1993, **72**, 519–537.